Progress in Earth and
Planetary Science

RESEARCH ARTICLE   **Open Access**

Biomarker records and mineral compositions of the Messinian halite and K–Mg salts from Sicily

Yuta Isaji[1]* , Toshihiro Yoshimura[1], Junichiro Kuroda[2], Yusuke Tamenori[3], Francisco J. Jiménez-Espejo[1,4],
Stefano Lugli[5], Vinicio Manzi[6], Marco Roveri[6], Hodaka Kawahata[2] and Naohiko Ohkouchi[1]

Abstract

The evaporites of the Realmonte salt mine (Sicily, Italy) are important archives recording the most extreme conditions of the Messinian Salinity Crisis (MSC). However, geochemical approach on these evaporitic sequences is scarce and little is known on the response of the biological community to drastically elevating salinity. In the present work, we investigated the depositional environments and the biological community of the shale–anhydrite–halite triplets and the K–Mg salt layer deposited during the peak of the MSC. Both hopanes and steranes are detected in the shale–anhydrite–halite triplets, suggesting the presence of eukaryotes and bacteria throughout their deposition. The K–Mg salt layer is composed of primary halites, diagenetic leonite, and primary and/or secondary kainite, which are interpreted to have precipitated from density-stratified water column with the halite-precipitating brine at the surface and the brine-precipitating K–Mg salts at the bottom. The presence of hopanes and a trace amount of steranes implicates that eukaryotes and bacteria were able to survive in the surface halite-precipitating brine even during the most extreme condition of the MSC.

Keywords: Messinian Salinity Crisis, Evaporites, Kainite, μ-XRF, Biomarker

Introduction

The Messinian Salinity Crisis (MSC) is one of the most massive evaporation events in Earth's history (Hsü et al. 1973; Rouchy and Caruso 2006; Ryan 2009; Roveri et al. 2014; and references therein). More than 1 million km^3 of salts precipitated over the Mediterranean basin between 5.97 and 5.33 Ma (Krijgsman et al. 1999), primarily driven by tectonically induced restriction of the Mediterranean–Atlantic gateway and gradual isolation of the Mediterranean Sea (Duggen et al. 2003). The MSC is divided into three stages, which correspond to the gypsum ($CaSO_4 \cdot 2H_2O$)–halite (NaCl)–gypsum trilogy observed mainly in the Eastern Mediterranean basin (Fig. 1a; Roveri et al. 2014), among which the halite phase accompanying occasional intercalation of highly soluble K–Mg salt layers represents the most extreme

hypersaline condition between 5.60 and 5.55 Ma (Manzi et al. 2009).

Previous studies have explored the relationships among the climate, the hydrological conditions, and the precipitating evaporites during the MSC peak, based on the distributions of mineral phases and elements in the evaporites (Garcia-Veigas et al. 1995; Lugli et al. 1999; Yoshimura et al. 2016), rhythmical alternation of the evaporitic sequences (Manzi et al. 2012), chemistry of the fluid inclusions in halite crystals (Rigaudier et al. 2011), and Os isotopic records (Kuroda et al. 2016). By contrast, much less is known on the responses of the biological communities, partly because evaporites generally do not contain microfossils commonly used in biogeochemical studies (Bertini et al. 1998). Based on the nitrogen isotopic compositions of geoporphyrins, which are derivatives of chloropigments, it has been suggested that the nitrogen cycle oscillated dynamically during the MSC peak, between a phase of active ammonium uptake by phototrophs and that dominated by evaporative degassing of ammonium under suppressed biological

* Correspondence: isajiy@jamstec.go.jp
[1]Biogeochemistry Program, Japan Agency for Marine-Earth Science and Technology, 2-15 Natsushima, Yokosuka, Kanagawa 237-0061, Japan
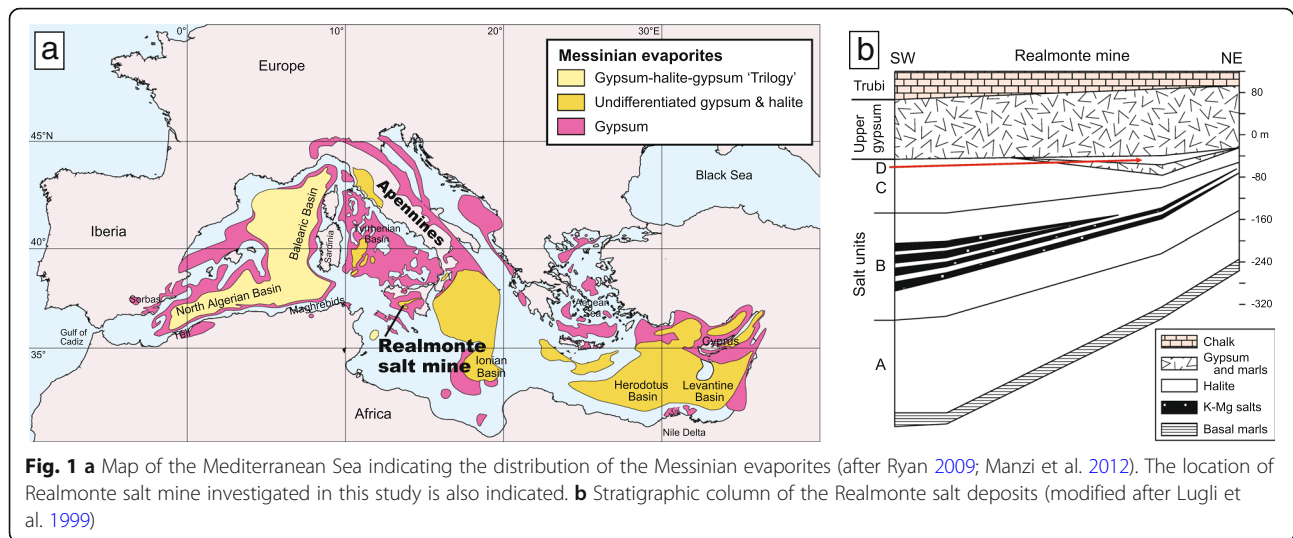Full list of author information is available at the end of the article

Fig. 1 a Map of the Mediterranean Sea indicating the distribution of the Messinian evaporites (after Ryan 2009; Manzi et al. 2012). The location of Realmonte salt mine investigated in this study is also indicated. **b** Stratigraphic column of the Realmonte salt deposits (modified after Lugli et al. 1999)

activity (Isaji et al. 2019a). Despite such a clear indication of substantial fluctuations in the biological activity, insights into the compositions of microbial communities are lacking. Such investigation is necessary in constraining the habitable limit of life during the massive evaporation events. Moreover, the transitions in the state and compositions of the microbial communities may in turn strongly affect the chemical characteristic of the evaporating brine. For example, biological activity strongly influences the CO_2 exchange between the brine and the atmosphere (Lazar et al. 1992; Isaji et al. 2017), and organic matter concentrated in the brine reduces the evaporation rate and the degree of evaporation that the brine can reach (Shalev et al. 2018).

While the massive halites deposited during the MSC peak are widely distributed in the deep Mediterranean basins (Fig. 1a; Lofi et al. 2011), the accessible archive is limited, one of which is the on-shore salt deposits of the Realmonte salt mine in the Caltanissetta Basin (Sicily, Italy). Here, we present and discuss the results of microscale elemental mapping and biomarker (i.e., source-specific organic molecules) distributions of the K–Mg salt layers and the shale–anhydrite–halite cyclical deposits. The K–Mg salt layers are among the most soluble evaporite found in the Realmonte salt mine, recording one of the most extreme evaporitic conditions during the MSC peak. The shale–anhydrite–halite triplets are the most representative cyclical deposits of the Realmonte salt mine (Decima and Wezel 1973; Lugli et al. 1999). Because the mineralogy of the evaporites is dependent on the chemical composition of the brine, the distribution patterns of the evaporite minerals provide fundamental information on the hypersaline environments. Among the biomarkers preserved in the evaporites, we specifically focused on lipid biomarkers, including long-chain (C_{25}–C_{36}) *n*-alkanes produced mainly by terrestrial

higher plants, insects, and fungi (Oro et al. 1966; Eglinton and Hamilton 1967), steroids constituting a major component in the cell membrane of eukaryotes (Volkman 2005; Summons et al. 2006), and hopanoids abundantly produced by bacteria as a cell membrane component (Rohmer et al. 1984; Ourisson and Albrecht 1992). This study will better constrain the biological and hydrological conditions during the MCS peak in the Caltanissetta Basin, which will be an important comparative data for understanding the environmental conditions in the entire Mediterranean basin during the MSC.

Geological setting

The Realmonte salt mine cuts through evaporites of the Caltanissetta Basin located in the southwest of Sicily (Fig. 1a), deposited during the peak of the MSC between 5.60 and 5.55 Ma (Manzi et al. 2009; Roveri et al. 2014). It belongs to the Gessoso-Solfifera Formation and lies above a gypsiferous/anhydritic unit considered to have deposited during stage 1 of the MSC (5.97–5.60 Ma) and is overlain by a marly succession that contains up to six gypsum beds (the Pasquasia Gypsum Member) (Decima and Wezel 1973; Garcia-Veigas et al. 1995; Lugli et al. 1999).

The salts in the Realmonte salt mine are divided into four main lithological units (A–D) from the base to the top (Fig. 1b; Decima and Wezel 1973; Lugli et al. 1999). Unit A is composed of plate cumulates of halite precipitated in a relatively deep-water setting. The overlying Unit B is composed of plate cumulates of halite in a shallowing upward sequence containing as many as 12 layers of K–Mg salts near the top of the unit. These layers are mainly composed of fine- to coarse-grained kainite ($MgSO_4 \cdot KCl \cdot 3H_2O$) that are cumulitic in origin (Garcia-Veigas et al. 1995). They have undergone deformation by tectonics with slump-like folding during or after the deposition, which acted differently on the salts

Isaji et al. Progress in Earth and Planetary Science   (2019) 6:60

Page 3 of 15

having specific rheological behavior compared to the surrounding rocks (Lugli et al. 1999). The halite layers in this unit show no evidence of bottom overgrowth, current structure, or dissolution and/or truncation surfaces, indicating that the halite precipitation occurred in a relatively deep-water setting below the wave base (Lugli et al. 1999). Upward shallowing of the basin occurred only in the uppermost halite layers of unit B, which is evidenced by large halite rafts together with localized dissolution pits filled by mud. The contacts between Unit B and C are characterized by the localized dissolution pits filled with mud, features that suggest desiccation of the basin and the formation of large expansion−contraction salt polygons (Lugli et al. 1999). Unit C, deposited after the basin had undergone desiccation, is composed of more than 120 lithological cycles, each one represented by the superposition of three main facies: (1) a millimeter-thick shale layer, (2) a millimeter−centimeter-thick anhydrite ($CaSO_4$) or polyhalite ($K_2MgCa_2(SO_4)_4 \cdot 2H_2O$) layer, and (3) a decimeter-thick halite layer with white patchy polyhalite grains (Lugli et al. 1999; Yoshimura et al. 2016). The highly pure halite cumulates of skeletal hoppers with chevron overgrowths indicate that the precipitation occurred in a relatively shallow, non-stratified water body during the dry season of the year, whereas the shale layers are considered to have deposited under a stratified water body during the wet season (Lugli et al. 1999; Manzi et al. 2012). Unit D is discontinuous and comprises halite and minor anhydrite, but it is not crossed by the mine and could not be described in detail.

Materials and methods
Sample collection
Rock samples of the Unit C shale−anhydrite−halite triplets were collected with a chisel and hammer from the 37th to 38th cycles above the erosional surface between Unit B and Unit C at "Church section" of the Realmonte salt mine (Manzi et al. 2012; Fig. 2h, i), which is located below 100 m from the ground level and over 1 km in horizontal distance from the exit of the mine. We also collected two fallen rock samples of K−Mg salts near the "Church section" where the outcrop of K−Mg salt layer in the upper part of Unit B is exposed (Fallen rock A and B; Table 1). The yellowish mineral surrounding the fallen rocks were similar in appearance to the K−Mg salt layer in the outcrop, indicating that these rocks originated from this layer. This layer was highly deformed, and the sedimentological features were lost (Fig. 2a−d).

Analytical procedures
Hydrocarbon biomarker analysis
Two fallen rock samples from K−Mg salt layer in Unit B (~100 g of Fallen rock A and ~ 70 g of Fallen rock B),

cycle 37th and 38th halite layers (~ 70 g each), and shale−anhydrite layers in between in Unit C (~ 10 g) were analyzed for hydrocarbon biomarkers. The outer parts of the rock samples were carefully eliminated with a chisel and hammer. The remaining inner parts were washed in Milli-Q water, methanol, and dichloromethane for 1 min each with sonication to eliminate any possible contaminants on the surface of the rock.

Each pulverized sample was extracted three times by sonication in dichloromethane:methanol (7:3, v/v) for 15 min. The total lipid extracts were saponified with 0.5 M KOH in methanol:H_2O (95:5, v/v) at 80 °C for 2 h. This was extracted then with n-hexane three times to obtain neutral lipids. Free hydrocarbon fraction (i.e., organic compounds not bound to macromolecules) was obtained by silica gel column chromatography using n-hexane:dichloromethane (95:5, v/v) as the solvent. The remaining saponified fraction was reacted with nickel boride to release S-bound compounds following the methodology of Schouten et al. (1993). First, the dried fraction was eluted in 4 mL methanol:tetrahydrofuran (1:1, v/v). A total of 200 mg $NiCl_2$ were added and stirred with a magnetic stirrer. Then, 100 mg $NaBH_4$ was added and reacted for 1 h at room temperature. This was extracted in n-hexane:NaCl-saturated-H_2O (1:1, v/v) to dissolve the released organic compounds in the n-hexane fraction. Sulfur-bound hydrocarbon fraction (desulfurized N-1) was obtained by silica gel column chromatography using n-hexane:dichloromethane (95:5, v/v) as the solvent. Both free and desulfurized N-1 fractions were eluted in n-hexane prior to the injection to gas chromatography/mass spectroscopy (GC/MS).

The GC/MS analysis was carried out using an Agilent Technologies (Santa Clara, CA, USA) model 7890A GC connected to a 5975C mass−selective detector. We used a VF-5ms fused silica capillary column (30 m × 0.25 mm i.d.; film thickness 0.1 μm) and helium as the carrier gas. The column oven temperature was programmed as follows: hold at 40 °C for 2 min, raise to 120 °C at 30 °C min^{-1}, then to 320 °C at 6 °C min^{-1}, and hold at 320 °C for 20 min. The PTV injector temperature was programmed as follows: hold at 50 °C for 0.3 min, raise to 350 °C at 600 °C min^{-1}, and hold at 350 °C for 10 min. Also, selected ion monitoring (SIM) of m/z = 217 (steranes) was performed for free and desulfurized N-1 fractions of the Fallen rock B sample. Identification of each compound was based on its retention time and mass spectrum. Blank experiments performed concurrently with the sample analysis showed no contamination that would affect the results.

μ-XRF, XANES, and XRD analyses
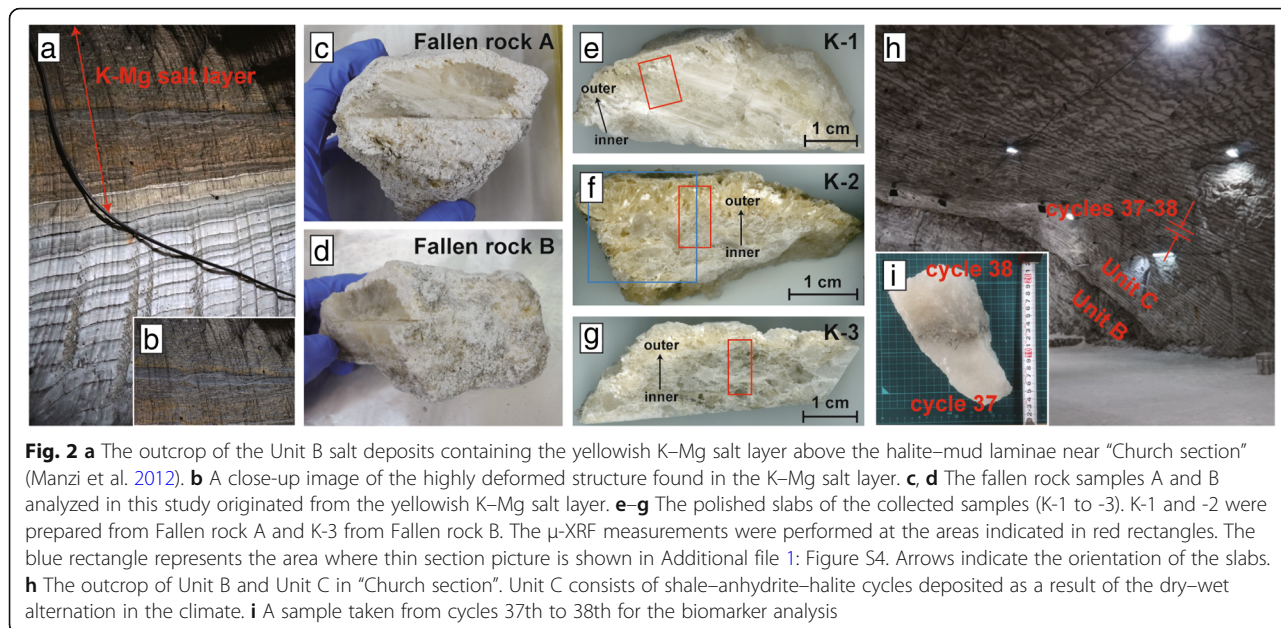The microscale elemental mapping of geological material is a commonly employed approach for identifying the

Fig. 2 a The outcrop of the Unit B salt deposits containing the yellowish K–Mg salt layer above the halite–mud laminae near "Church section" (Manzi et al. 2012). **b** A close-up image of the highly deformed structure found in the K–Mg salt layer. **c, d** The fallen rock samples A and B analyzed in this study originated from the yellowish K–Mg salt layer. **e–g** The polished slabs of the collected samples (K-1 to -3). K-1 and -2 were prepared from Fallen rock A and K-3 from Fallen rock B. The μ-XRF measurements were performed at the areas indicated in red rectangles. The blue rectangle represents the area where thin section picture is shown in Additional file 1: Figure S4. Arrows indicate the orientation of the slabs. **h** The outcrop of Unit B and Unit C in "Church section". Unit C consists of shale–anhydrite–halite cycles deposited as a result of the dry–wet alternation in the climate. **i** A sample taken from cycles 37th to 38th for the biomarker analysis

depositional environments (e.g., Yoshimura et al. 2016). The high-sensitivity scanning X-ray fluorescence (XRF) that utilizes synchrotron radiation sources with X-ray focusing optics (i.e., μ-XRF) has the advantage of generating trace element distributions with a micrometer-scale spatial resolution (e.g., Sutton et al. 2002; Tamenori et al. 2014). In addition, the use of energy-tunable synchrotron radiation allows chemical speciation by X-ray absorption near edge structure (XANES) (e.g., Spiro et al. 1984; Yoshimura et al. 2015), which can be used to constrain the phases involved in compositionally complex materials like geologic materials.

Three 5 mm-thick slabs of the K–Mg salts were prepared from two fallen rock samples with a saw for μ-XRF measurement (herein referred to as K-1, K-2, and K-3; K-1 and K-2 prepared from Fallen rock A and K-3 from Fallen rock B; Fig. 2c–g). The cut surfaces were polished and then cleaned in an ultrasonic bath with hexane. After the X-ray analysis, thin sections of K-2 were prepared to describe the sedimentary structures. The sample was mounted on a glass slide and ground smooth.

All X-ray analysis was conducted at the b-branch of the soft X-ray photochemistry beamline (BL27SU) at the

SPring-8 synchrotron radiation facility (Hyogo, Japan), using monochromatized soft X-ray beam with a silicon drift detector (SDD) (Tamenori et al. 2011; Tamenori et al. 2014). The radiation from the undulator was monochromatized by using a double crystal Si(111) monochromator ensuring an energy resolution of 350 meV. Photon flux on the sample was 1×10^{11} Ph s^{-1} at sulfur K-edge. The Kirkpatrick–Baez mirror focused the photon beam on the sample, and the horizontal and vertical beam size at focus point were 16.3 and 13.7 μm, respectively.

For μ-XRF measurements, the polished slab was fixed on an aluminum sample holder that was then installed in a vacuum chamber and fixed on a motorized XYZ stage. The μ-XRF measurements were taken at a photon energy of 3000.0 eV with an acquisition time of 1 s at 100 μm intervals for both the horizontal and vertical axes. All XRF data were obtained at each mapping point, and the elemental imaging data were extracted from the XRF dataset. The reproducibility for signal intensities based on repeated analysis on the standard material was typically less than 5% (± 2σ) over ten replicates.

Sulfur K-edge μ-XANES measurements were performed using a two-dimensional approach for the partial fluorescence yield (PFY) measurement with an SDD in

Table 1 Samples from Realmonte salt mine analyzed in this study

Location	Deposits	Sample position	Subsamples	Analyses
Unit B near "Church section"	K–Mg salts	Fallen rock A	K-1, K2	XAFS, XRD, biomarker, thin section
		Fallen rock B	K-3	
Unit C "Church section"	Halite-anhydrite-mud	Cycle 37th–38th	37th halite	Biomarker
			37/38th shale-anhydrite	
			38th halite	

the soft X-ray region (Tamenori et al. 2011). The sample and detector layout for S-XANES was the same as that employed for the μ-XRF measurements. The selected energy range for S-XANES measurements was 2460–2510 eV with an energy step of 0.2 eV, and an acquisition time of 1 s step^{-1}. Five spots were analyzed for K-1 (spots 1-1–1-5) and four spots each for K-2 and -3 (spots 2-1–2-4 and 3-1–3-4).

The evaporite minerals composing the samples were further confirmed by X-ray diffraction (XRD) analysis using PANanalytical X'Pert Pro X-ray diffractometer (PANalytical B.V., Almelo, the Netherlands). Single crystals of each evaporite mineral, which were determined by μ-XRF and XANES, were collected from K-2 with a dental drill, and powdered using agate mortar prior to the analysis.

Results and discussion
Sedimentary facies and spatial distribution of elements of Unit B K–Mg salt layer
While the outer parts of the fallen rock samples and the surface of the outcrop of the K–Mg salt layers in Unit B were both covered by yellowish mineral ~ 1 cm-thick, the cut surface of the K–Mg salt slabs showed transparent and whitish crystals in the inner part (Fig. 2c–g). Elemental mapping by μ-XRF revealed a similar distribution pattern of elements for all slabs (Fig. 3, Additional file 1: Figures S1 and S2). Compared to the main peaks of the sulfur K-edge XANES spectra of the reference compounds shifting toward higher energies with increasing valent state (Fig. 4), all spectra of the K–Mg salts exhibited a pronounced peak at around 2482 eV, indicating that sulfur is predominantly in a fully oxidized state (S^{6+}). The evaporite minerals comprising the slabs are identified as follows:

1. The major elements composing the most abundant mineral of the inner part of the slabs were Mg, O, S, and Cl (Fig. 3, Additional file 1: Figures S1 and S2). The S μ-XANES spectra obtained from the measurement points 1-1, 1-2, 2-2, and 3-4 exhibited a pronounced peak appearing at 2482 eV and some resonances at around 2486.5, 2491, 2494.5, and 2499 eV in the post-edge regions (Fig. 4), which is identical with the spectrum of kainite reported previously (Yoshimura et al. 2016). The XRD analysis also confirms this mineral as kainite (Additional file 1: Fig. S3).

2. Minerals composed of Na and Cl were also distributed in the inner part of the K–Mg salt rocks (Fig. 3, Additional file 1: Figure S1 and S2), which was identified as halite (Additional file 1: Figure S3). Although any primary sedimentary structures with detrital textures and fabrics were not recognized in the thin section of K-2, the halite crystals contained fluid-inclusion-rich bands alternating with fluid-

inclusion-poor bands (Additional file 1: Figure S4), a primary subaqueous texture indicating that they are of primary origin precipitated at the brine surface as the halite rafts (Lowenstein and Hardie 1985; Garcia-Veigas et al. 1995; Lugli et al. 1999). The cross plots of Al, Si, and P indicate that the signal intensities of these elements are higher and varies within a narrow range in the halite phase compared to other mineral phases (Fig. 5). The high correlations between these elements imply that these signals derive from aluminosilicate clay minerals, with P present as adsorbed inorganic and organic P on the surface of the clay minerals and/or as aluminum oxides (e.g., Shen et al. 2011). The S μ-XANES spectra obtained at the measurement spots 2-1 and 3-1 unambiguously indicate the co-existence of sulfate compounds in the halite crystals (Fig. 4). However, a low signal-to-noise ratio in the μ-XANES analyses did not permit us to find conclusive evidence concerning the average local structural and compositional environment of sulfate in halite.

3. The minerals surrounding the outer part of the slab which are found as vertically oriented needle crystals mostly having euhedral to subhedral shapes (Additional file 1: Figure S4) contained O, S, and Mg (Fig. 3, Additional file 1: Figures S1 and S2). The XRD analysis identified this mineral as leonite ($K_2Mg(SO_4)_2 \cdot 4H_2O$) (Additional file 1: Figure S3). The S-XANES spectra of leonite at the measurement spots 1-4, 1-5, 2-3, 2-4, 3-2, and 3-3 exhibited a pronounced peak in the post-edge region appearing at 2494 and 2499 eV, and resonance on the high-energy side of highest peaks appeared at 2485.5 and 2488.5 eV (Fig. 4).

Thus, kainite, halite, and leonite are the main minerals composing the K–Mg salt slabs, among which halite is of primary origin. Both kainite and leonite can be precipitated from the seawater as primary mineral or formed as secondary mineral by dissolution–reprecipitation of the bittern salts (Stewart 1963; Bąbel and Schreiber 2014). The distribution of leonite surrounding the outer rims of our rock samples suggests them as the secondary diagenetic mineral. On the other hand, although the kainite grains of the Unit B K–Mg salt layers show pressure–dissolution feature (Garcia-Veigas et al. 1995; Lugli et al. 1999) indicating that at least the rims of the kainite crystals have undergone post-burial alteration, the observations in this study could not provide conclusive evidence on their origin. Thus, kainite may be of primary origin precipitated from the brine, or they may have been recrystallized from other K–Mg salt minerals such as sylvite (KCl), carnallite ($KCl \cdot MgCl_2 \cdot 6H_2O$), or
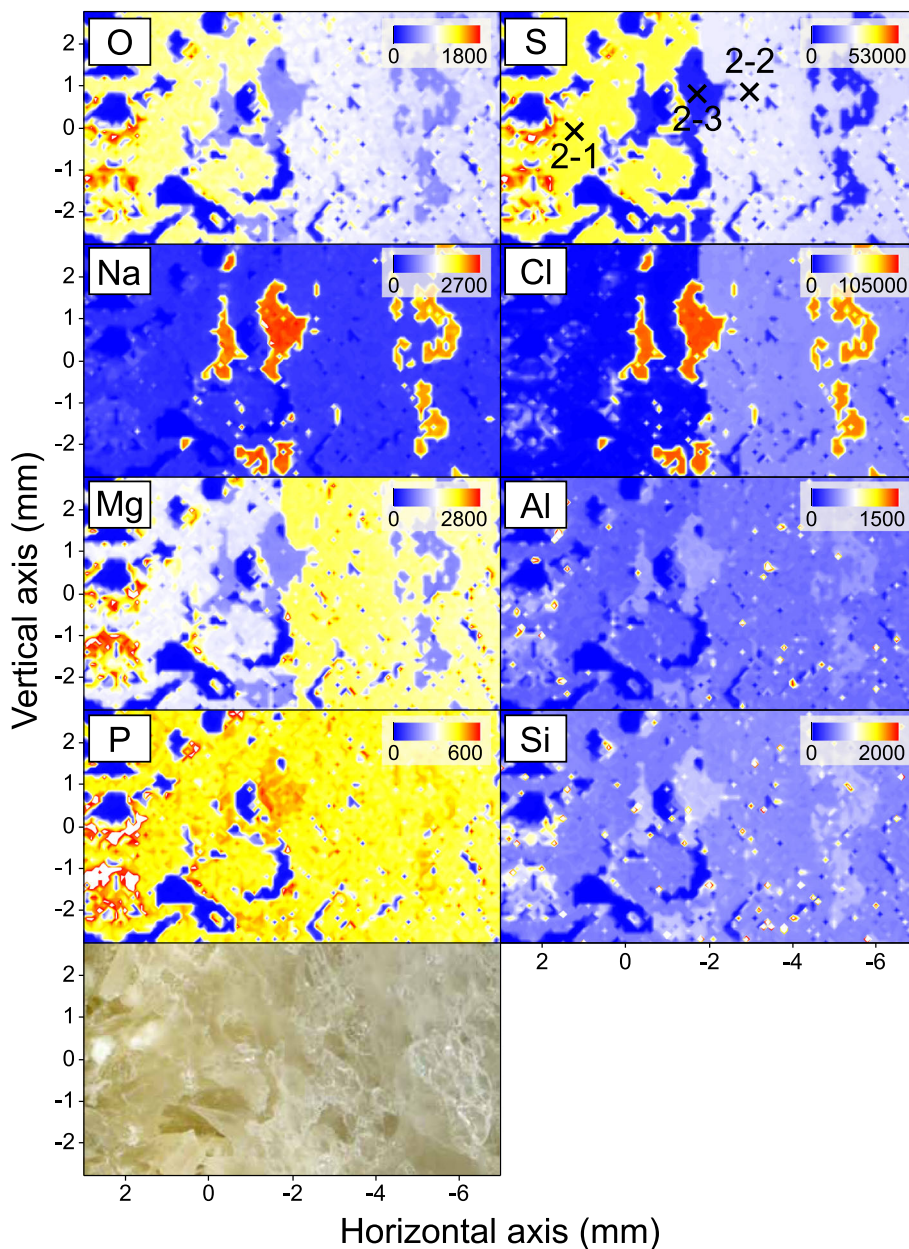
Fig. 3 The μ-XRF intensity maps of O, S, Na, Cl, Mg, Al, P, and Si, together with the picture of the measured area in K-2. Color scales indicate element concentrations in signal counts per second. Black crosses in the μ-XRF intensity map of S denote μ-XANES measurement points

kieserite ($MgSO_4 \cdot H_2O$) (Stewart 1963). Either primary or secondary in origin, their presence at least indicates that the salinity of the brine in the Caltanissetta basin exceeded the saturation point of the K–Mg salts during the MSC peak, which is over 70 times concentration of the seawater (Warren 2016; Shalev et al. 2018).

The biomarker assemblages and their origins
Unit C shale–anhydrite–halite triplets
The distribution of organic compounds in the halite phases of Unit C cycles 37th and 38th were similar, thus

only the chromatograms of the cycle 37th halite layer are indicated (Fig. 6 and Table 2). All samples analyzed contained abundant S-bound organic compounds, suggesting the presence of reduced sulfur species (e.g., sulfide, elemental sulfur, polysulfides) in the water column and/or porewater generally supplied by sulfate reduction driven under anoxic condition (Werne et al. 2004). Gammacerane, derived from tetrahymanol produced by bacterivorous anaerobic ciliates (Sinninghe Damsté et al. 1995a; Takishita et al. 2012), was indeed detected from the shale–anhydrite layer of the Unit C (Fig. 6c; peak
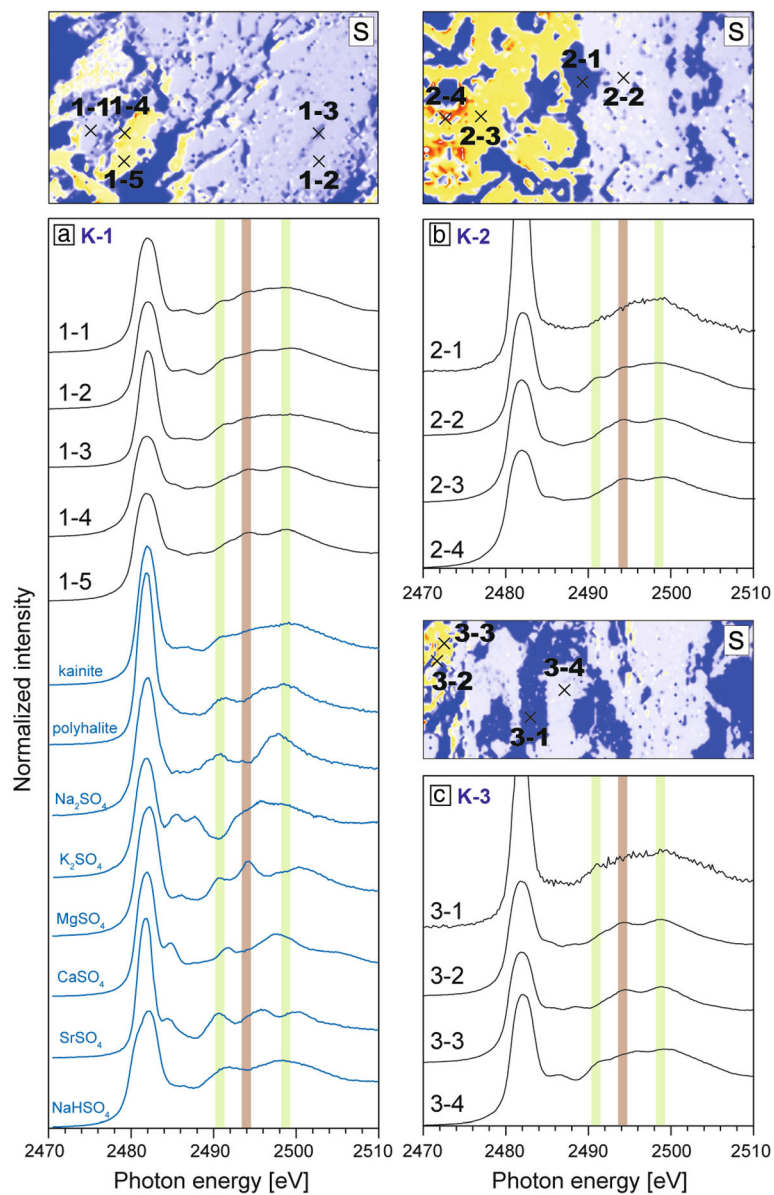
Fig. 4 a–c Sulfur *K*-edge XANES spectra of the K–Mg salt slabs. Micro-XANES measurements were performed at the focused mode at each measurement point. Black crosses in the μ-XRF intensity map of S denote μ-XANES measurement points. The spectra for reference materials (blue lines) are from Yoshimura et al. (2013)

12), which suggests the formation of bottom water anoxia as a result of density stratification between brines with different salinity (Manzi et al. 2012). The lack of gammacerane in the Unit C halite layers and the Unit B K–Mg salt layer do not necessarily indicate the absence of anoxic bottom water, because the salinity may have been too high for bacterivorous anaerobic ciliates to inhabit. Considering the upper salinity limit of the sulfate-reducing bacteria in culture (240 g L^{-1}: Oren 2002), the reduced sulfur species used to form S-bound organic compounds in the halite and K–Mg salts may have been

originally produced when freshwater–brine stratification was formed.

While *n*-alkanes were not detected in free N-1 fraction of the Unit C halite layer, the desulfurized N-1 fraction contained C$_{18}$–C$_{29}$ *n*-alkanes characterized by a strong even carbon-number predominance for C$_{18}$–C$_{22}$ (Fig. 6a, b). Because a functional group or unsaturated sites are necessary for an organic compound to become S-bound, these C$_{18}$–C$_{22}$ *n*-alkanes are derived probably from alkyl lipids such as fatty alcohols and fatty acids of marine organisms (Naraoka and Ishiwatari 2000; Schouten et al.
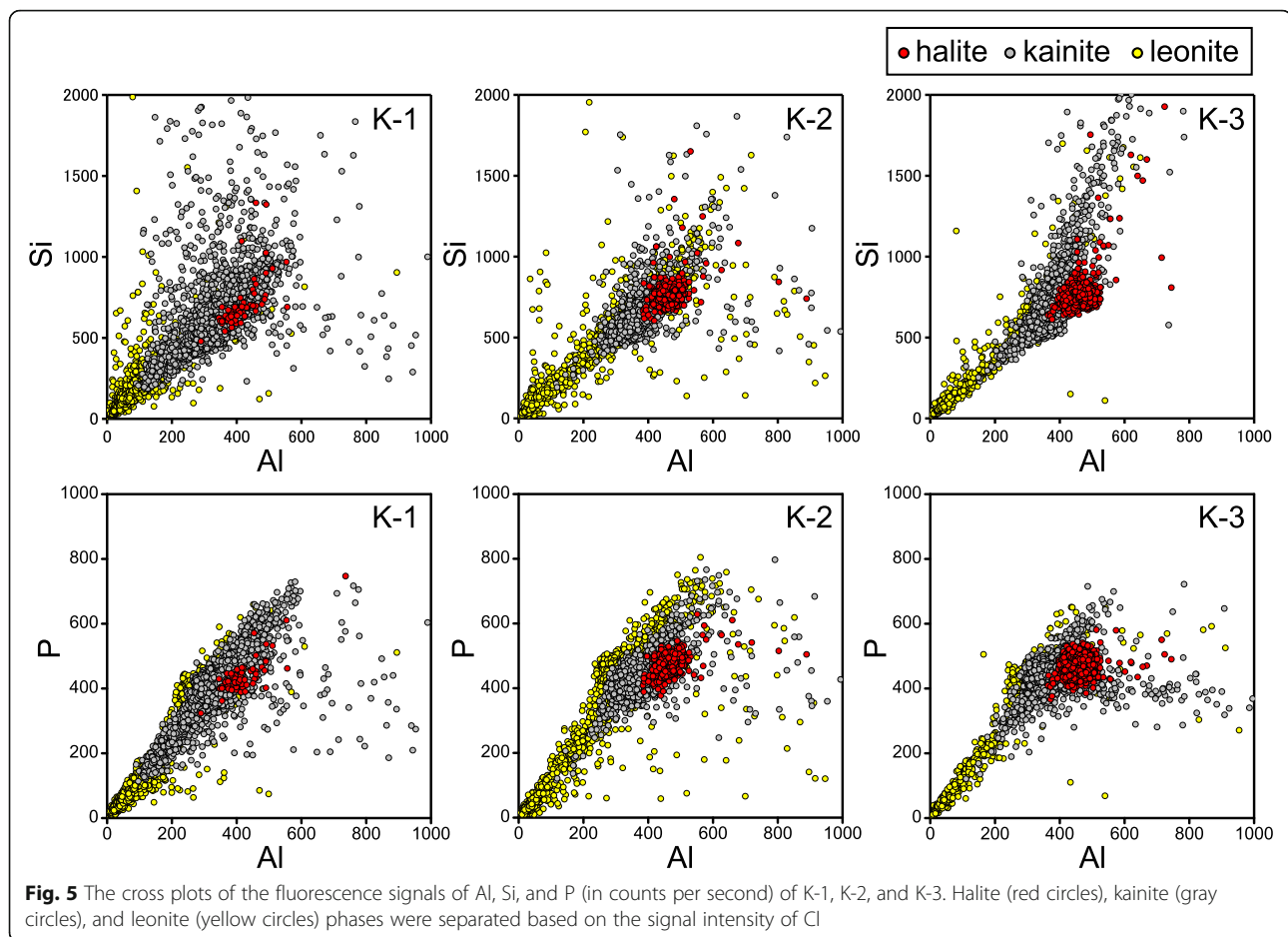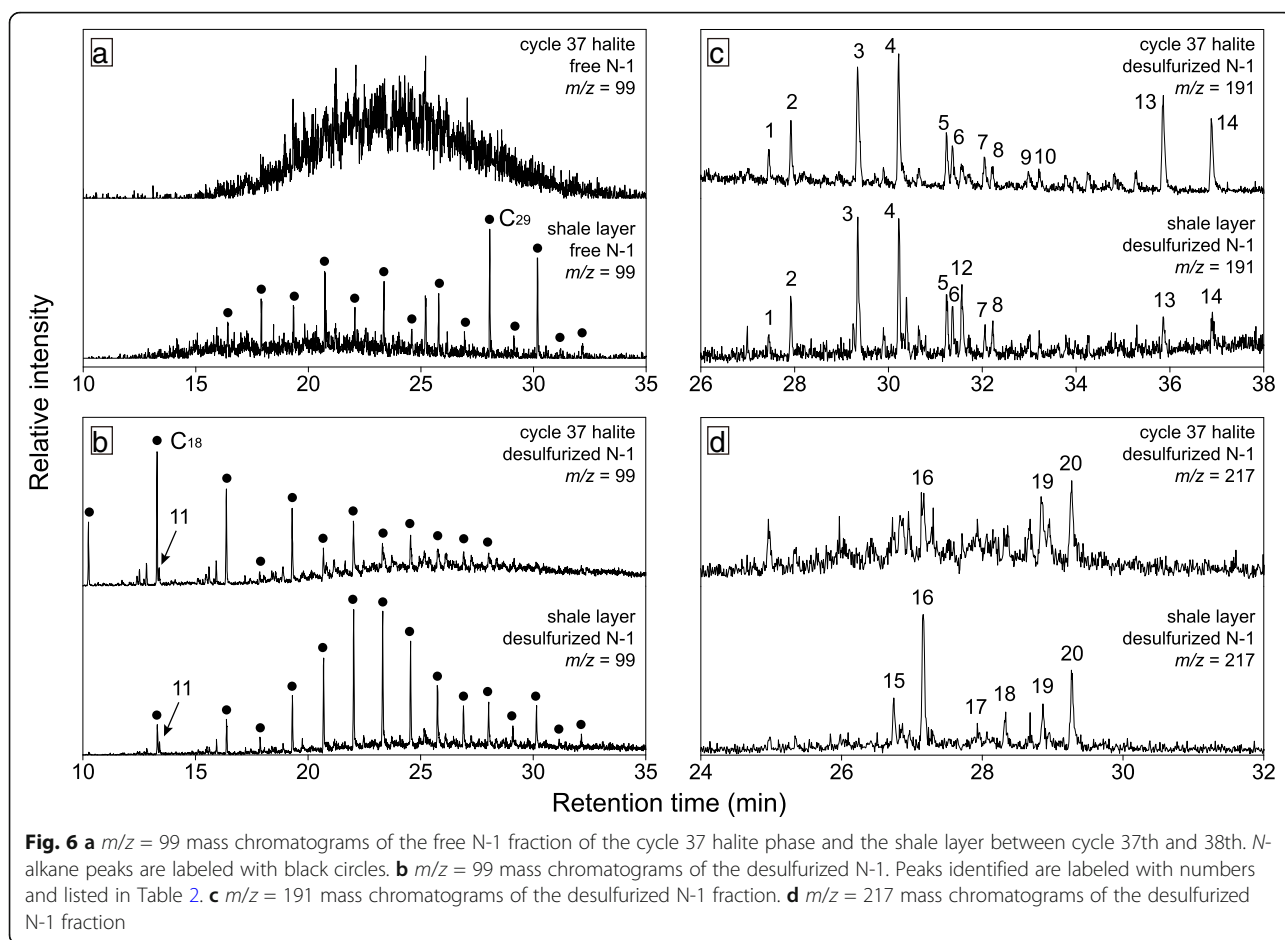
Fig. 5 The cross plots of the fluorescence signals of Al, Si, and P (in counts per second) of K-1, K-2, and K-3. Halite (red circles), kainite (gray circles), and leonite (yellow circles) phases were separated based on the signal intensity of Cl

2001; Bergé and Barnathan 2005). By contrast, a strong odd carbon-number predominated long-chain (i.e., C_{25}–C_{36}) n-alkanes in the free N-1 fraction of the shale–anhydrite layer of the Unit C (Fig. 6a) are derived from terrestrial organisms such as higher plants, insects, and fungi (Oro et al. 1966; Eglinton and Hamilton 1967), which are likely to have been transported together with the continental water inflow supplied during the deposition of shale layers (Manzi et al. 2012).

Hopanes and steranes preserved in the deposits are potentially informative biomarkers for paleoenvironmental studies. Hopanes are degradation products of hopanoids, which are pentacyclic triterpenes abundantly produced by bacteria as a cell membrane component (Rohmer et al. 1984; Ourisson and Albrecht 1992). Steranes, on the other hand, are molecular indicators of eukaryotes, as their biosynthetic process requiring molecular oxygen is found almost exclusively in eukaryotes (Volkman 2005; Summons et al. 2006). Because of the ubiquity of eukaryotes and bacteria in normal marine environments, hopanes and steranes are preserved in almost any geological materials. However, their presence or absence under extreme environments could provide valuable insights, although it

should be kept in mind that such discussions are based on the assumptions that the degradation rate and sulfur-binding efficiency of the steranes and hopanes are comparable.

The chromatograms of the fragment ion $m/z = 191$ showed that both free and desulfurized N-1 fractions of the Unit C halite and shale–anhydrite layers contained $17\alpha(H)$- and $18\alpha(H)$-isomers of trisnorhopanes, $17\alpha(H)$, $21\beta(H)$ isomers of norhopane and hopane, C_{31} to C_{33} $17\alpha(H),21\beta(H)$-homohopanes with both 22S and 22R configurations (22S:22R = 3:2), and $17\beta(H),21\beta(H)$ isomers of C_{34} and C_{35} homohopanes (Fig. 6c). The chromatograms of the fragment ion $m/z = 217$ indicated the presence of C_{27}–C_{29} sterane homologs with both $5\alpha(H)$ and $5\beta(H)$ isomers in the desulfurized N-1 fractions of the halite and shale–anhydrite layers of Unit C (Fig. 6d). Hopanes and steranes have similarly been reported from other MSC deposits, such as carbonate deposits and organic-rich marls (e.g., Sinninghe Damsté et al. 1995b; Guido et al. 2007; Birgel et al. 2014; Natalicchio et al. 2017), and gypsums deposited during stage 1 of the MSC (ten Haven et al. 1985; Schouten et al. 2001; Isaji 2018). Our study reports here for the first time the presence of steranes in evaporites precipitated above the

Fig. 6 a m/z = 99 mass chromatograms of the free N-1 fraction of the cycle 37 halite phase and the shale layer between cycle 37th and 38th. N-alkane peaks are labeled with black circles. **b** m/z = 99 mass chromatograms of the desulfurized N-1. Peaks identified are labeled with numbers and listed in Table 2. **c** m/z = 191 mass chromatograms of the desulfurized N-1 fraction. **d** m/z = 217 mass chromatograms of the desulfurized N-1 fraction

saturation point of halite (concentrated over 10 times of the seawater).

Several criteria must be met before hopanes and steranes can be used as biomarkers of organisms inhabiting the water column. Due to their wide occurrence in the contemporary natural environment, hopanes and steranes could be "contaminants" added after the deposition of evaporites. Thus, the criteria for their use as the biomarkers of eukaryotes and bacteria is whether these organic compounds are syngenetic with the associated deposits (Hayes et al. 1983). In the face of such a problem, the stereochemistry of hopanes can be used to

Table 2 Hydrocarbon compounds identified in this study

Peak	Compound	Peak	Compound
1	18α(H)-trisnorhopane*	11	Phytane
2	17α(H)-trisnorneohopane*	12	Gammacerane
3	17α(H), 21β(H)-norhopane	13	C_{34}-17β(H), 21β(H)-homohopane
4	17α(H), 21β(H)-hopane	14	C_{35}-17β(H), 21β(H)-homohopane
5	C_{31}-17α(H), 21β(H)-homohopane (22S)	15	C_{27}-5β(H)-sterane
6	C_{31}-17α(H), 21β(H)-homohopane (22R)	16	C_{27}-5α(H)-sterane
7	C_{32}-17α(H), 21β(H)-homohopane (22S)	17	C_{28}-5β(H)-sterane
8	C_{32}-17α(H), 21β(H)-homohopane (22R)	18	C_{28}-5α(H)-sterane
9	C_{33}-17α(H), 21β(H)-homohopane (22S)	19	C_{29}-5β(H)-sterane
10	C_{33}-17α(H), 21β(H)-homohopane (22R)	20	C_{29}-5α(H)-sterane

*Tentative assignments

distinguish the hopanoids of living organisms and their fossil counterparts. The biological stereochemistry of hopanoids ($22R$-17β(H),21β(H) isomer) are progressively degraded and stereochemically altered upon burial, leading to the dominance of 17α(H),21β(H) configuration with $22S/22R$ ratio ~ 3:2 at advanced levels of maturity (Ourisson and Albrecht 1992). Thus, the stereochemical patterns of C_{29} to C_{33} hopanes in all of our samples clearly eliminate their origin from the recent bacterial source. The presence of biological isomers of hopanes (C_{34} and C_{35} 17β(H),21β(H)-homohopanes) in the halite layers of Unit C is enigmatic. Although speculative, they may originate from bacteria trapped in the fluid inclusions of the halite crystals, which are reported to survive on a geological timescale (McGenity et al. 2000; Lowenstein et al. 2011).

Another point that should be evaluated is whether these biomarkers are of terrestrial or aquatic origin. The contribution of terrestrially-derived steranes can be distinguished by the relative abundance of C_{29} steranes to C_{27} counterparts, because β-sitosterol, which degrades to C_{29} sterane, is abundantly produced by various terrestrial higher plants (Huang and Meinschein 1979). Thus, the higher abundance of C_{27} steranes relative to C_{29} counterparts in the Unit C shale–anhydrite layer (C_{27}/C_{29} ratio ~ 1.1) implies aquatic eukaryotes as their main biological source (Fig. 6d), which is consistent with the continental water inflow during its deposition (Manzi et al. 2012) because the lowering of salinity is likely to have relieved the salinity stress of eukaryotes which are less tolerable to a hypersaline condition compared to bacteria and archaea. The C_{27}/C_{29} sterane ratio was lower, ~ 0.5, for the Unit C halite layers. However, the abundance of terrestrial long-chain n-alkanes in these layers were below detection limit, which argues against terrestrial higher plants as the major origin of steranes. A possible source of steranes in the halite layers is the green alga *Dunaliella salina*, which is the only eukaryotic algae in the modern solar saltern ponds tolerable to salinity above the saturation point of NaCl (Oren 2002). Interestingly, *D. salina* grown at 0.6, 1.4, and 2.1 M predominantly produce C_{29} sterols (C_{27}/C_{29} ratio ~ 0.01; Francavilla et al. 2010), while C_{27} sterols are mainly synthesized by that grown at ~ 4 M NaCl (Kelly 2009). Although speculative, the relatively low C_{27}/C_{29} sterane ratio may reflect the predominance of *D. salina* among eukaryotic microorganisms during the halite deposition.

The relative peak intensities of hopanes and steranes were comparable for the shale–anhydrite layer (Fig. 6c, d). Inhabitance of eukaryotes during its deposition is reasonable considering the presence of less-saline layer in the surface of the water column. Clear peaks of hopanes and steranes are similarly detected from MSC gypsums (ten Haven et al. 1985; Schouten et al. 2001;

Isaji 2018). By contrast, the relative peak intensities of steranes with respect to hopanes were substantially reduced in the Unit C halite layers. This implies that the inhabitance of eukaryotes was gradually suppressed as the salinity increased from the saturation point of gypsum to that of the halite.
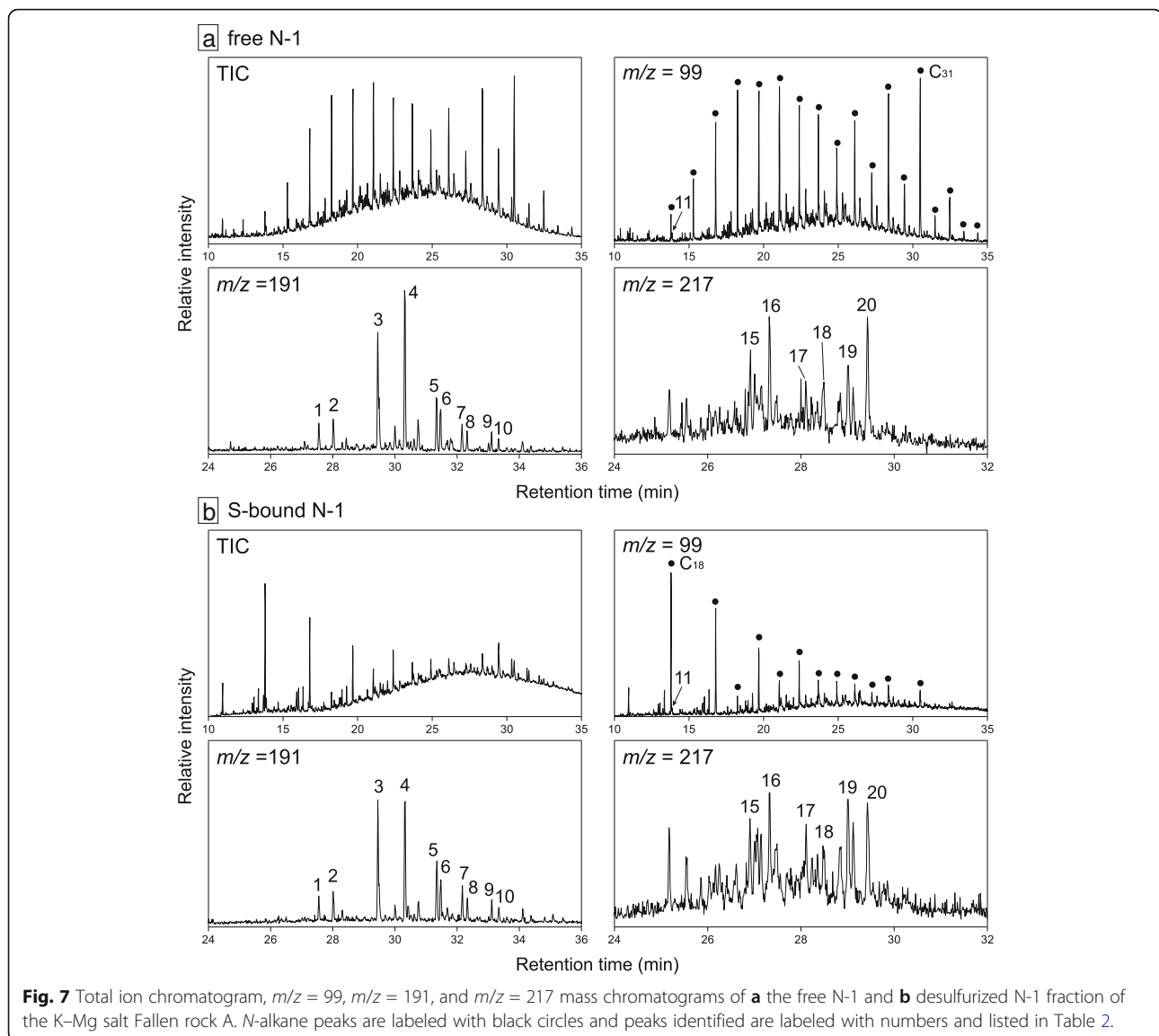
Unit B K–Mg salt layer

Among the biomarkers detected from the K–Mg salts, n-alkanes showed clearly different distribution patterns between the two fallen rock samples (Figs. 7, 8 and Table 2). While only C_{18}–C_{27} n-alkanes were detected from the Fallen rock B, an odd carbon-number predominated long-chain n-alkanes were present in the free N-1 fraction of the Fallen rock A, implying terrigenous organic matter input. On the other hand, the distributions of hopanes in free and desulfurized fractions of the two rock samples were similar to the Unit C samples, except for the absence of C_{34} and C_{35} 17(H)β,21β(H)-homohopanes. Both fallen rocks also contained trace amount of C_{27}–C_{29} steranes, although those in Fallen rock B were only detectable with the more-sensitive SIM analysis mode (Fig. 8). The homologous distributions of steranes in these K–Mg salts were similar to that of the Unit C halite layers.

Therefore, while the distribution of some classes of biomarkers (e.g., n-alkanes) are inhomogeneous, we consider that the clearly detectable amount of hopanes and a contrastingly lower amount of steranes are the characteristics of the K–Mg salt layers near the "Church section" in the Realmonte salt mine. The steranes detected in the Fallen rock A sample could potentially derive from terrestrial eukaryotic organisms such as plants, because long-chain n-alkanes indicative of terrigenous organic matter were also contained in this sample. On the other hand, steranes present in trace amount in Fallen rock B could have derived from aquatic eukaryotes, in particular, *D. salina* as similarly discussed in the previous section for the Unit C halite layers. Thus, our results imply that not only bacteria but also eukaryotes were present at least temporarily in the brine during the deposition of the K–Mg salt layer.

Depositional environment of Unit B K–Mg salt layer

Theoretically, the halites and K–Mg salts composing the Unit B K–Mg salt layer could have co-precipitated from a homogenous brine, because both halite and K–Mg salts can precipitate from brine concentrated over 70 times upon evaporation from the normal seawater (Warren 2016; Shalev et al. 2018). However, this is unlikely considering the presence of hopanes and steranes (Figs. 7 and 8), because the $MgCl_2$ concentration of the brine will be well above the habitable limit (~ 2.3 M: Hallsworth et al. 2007). Thus, the possible mechanisms

Fig. 7 Total ion chromatogram, *m/z* = 99, *m/z* = 191, and *m/z* = 217 mass chromatograms of **a** the free N-1 and **b** desulfurized N-1 fraction of the K–Mg salt Fallen rock A. *N*-alkane peaks are labeled with black circles and peaks identified are labeled with numbers and listed in Table 2.

explaining the mineral composition of the K–Mg salt layer include (1) allochthonous origin of either halite or K–Mg salts, (2) progressive evaporation of the brine from the saturation point of halite to that of K–Mg salts, and (3) the formation of temporal or persistent density stratification between halite-precipitating brine at the surface and brine-precipitating K–Mg salts at the bottom. Allochthonous transport of the K–Mg salts from the shallow margins to the halite-precipitating inner basin has indeed been proposed for the Na–Mg sulfate layer in Unit B of the Realmonte salt mine (Yoshimura et al. 2016). Nevertheless, this mechanism involves detrital materials filling the intergranular matrix (Yoshimura et al. 2016), which is not observed in our samples (Fig. 3, Additional file 1: Figsure S1, S2, and S4). Regarding possibility (2), it is highly improbable that a complete mineralization sequence from halite to K–Mg salt

saturation would be recorded in the analyzed area (< 1 cm, Fig. 2) considering the abundance of halite that precipitates during the course of seawater evaporation (Friedman and Sanders 1978).

Therefore, the most likely explanation is possibility (3), with eukaryotes and bacteria inhabiting in the halite-precipitating surface brine formed under temporal or persistent density stratification. An extremely low concentration of steranes implies that the salinity of this brine was much higher than the saturation point of halite, substantially reducing the population of eukaryotes. In such an extreme salinity, the evaporation rate and the amount of halite precipitated from the brine are low (Friedman and Sanders 1978). The resulting low precipitation rate of the halite crystals in the surface brine may explain the elevated concentration of Al, Si, and P derived from aluminosilicate clay minerals in the halite
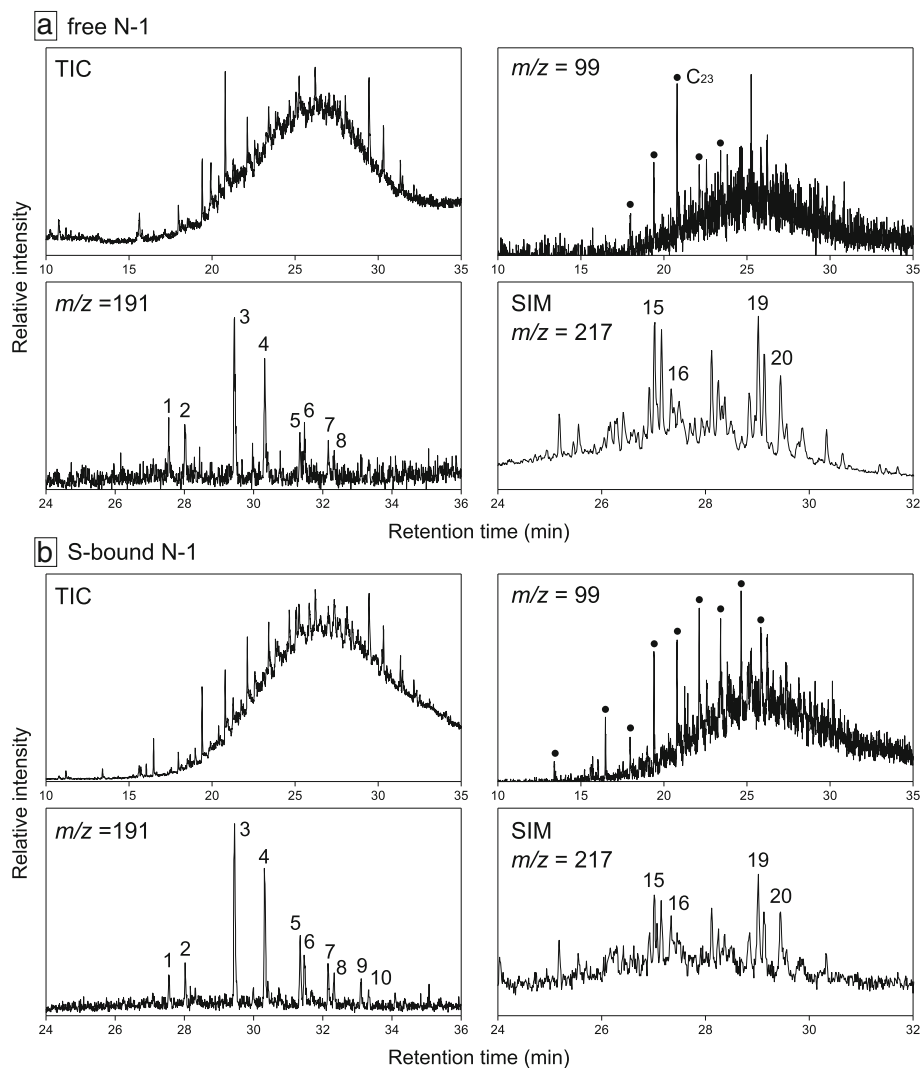
Fig. 8 Total ion chromatogram, *m/z* = 99, *m/z* = 191, and *m/z* = 217 mass chromatograms of (a) the free N-1 and (b) desulfurized N-1 fraction of the K–Mg salt Fallen rock B. Mass chromatograms of *m/z* = 217 were obtained by selected ion monitoring (SIM) mode. *N*-alkane peaks are labeled with black circles and peaks identified are labeled with numbers and listed in Table 2.

phase (Figs. 3 and 5, Additional file 1: Figures S1 and S2). In addition, this halite-precipitating surface brine may have been further diluted by episodic freshwater supply such as storms, which must have temporarily relived organisms from salinity stress. Such an occasional event may have produced inhomogeneous distribution of some biomarkers among different K–Mg salt rock samples, including terrestrial long-chain *n*-alkanes (Figs. 7 and 8). Indeed, blooming of eukaryotic phototroph *D. salina* have been reported in the upper layers of the Dead Sea after the storm events (Oren 2014).

The obtained data suggest for the first time the presence of eukaryotes and bacteria during the deposition of the K–Mg salt layer. They were able to survive even the most extreme condition of the MSC in the halite-

precipitating brine at the surface formed as a result of density stratification and/or possibly an episodic dilution of surface brine by freshwater. As the stratigraphic correlation between the marginal and deep Mediterranean basins is still inconclusive, it is difficult, at present, to extrapolate our conclusions to the entire Mediterranean basin. Nevertheless, our results will be an important comparison for the future drilling of cores from deep Mediterranean basin (e.g., MEDSALT initiative, https://medsalt.eu). Similar investigations for the cores from deep Mediterranean basin would reveal a lateral transition in key biogeochemical parameters such as salinity, microbial communities, and water column structure from the on-shore to off-shore basins. Such geochemical constraints on the water column structures are essential in understanding the hydrology and the spatial

distribution of evaporites in the Mediterranean basin (e.g., Simon and Meijer 2017). Moreover, while the impact of MSC on global climate has been discussed focusing on its influence on the ocean circulation (Ivanovic et al. 2014; Capella et al. 2019), changes in the microbial communities and water column structures within the Mediterranean basin may also have global impact through their influences on the biogeochemical cycle. For example, efficient nutrient recycling and density stratification during the MSC is suggested to have resulted in efficient carbon burial (Isaji et al. 2019a,b), which have the potential to influence the global carbon cycle. Such investigations for both on-shore and off-shore deposits will lead to comprehensive understanding of the global impact of MSC.

Conclusions The μ-XRF elemental mapping and mineral identification by S K-edge XANES and XRD, as well as thin section observation revealed that the K–Mg salt layer in Unit B of the Realmonte salt mine is composed of primary halite, diagenetically-formed leonite, and primary and/or secondary kainite. These minerals are interpreted to have precipitated from a density-stratified water column, with halite-precipitating brine at the surface and brine-precipitating K–Mg salts at the bottom. Eukaryotes and bacteria, the source of steranes and hopanes detected from the K–Mg salt layer, should have been inhabiting the halite-precipitating brine in the surface, because the $MgCl_2$ concentration in the bottom brine-precipitating K–Mg salts is well above their habitable limits. Temporal density stratification between brines with different salinity may have formed a temporal refuge for the microbial communities during the most extreme conditions of the MSC. Both steranes and hopanes are present in the Unit C shale–anhydrite–halite triplets, suggesting that both eukaryotes and bacteria persisted throughout this unit. Future deep-sea drilling of MSC evaporites would resolve whether the obtained conclusions are representative of the entire Mediterranean or just applicable to shallow restricted basins.

Additional files

Additional file 1: Figure S1. The μ-XRF intensity maps of O, S, Na, Cl, Mg, Al, P, and Si, together with the picture of the measured area in K-1. Color scales indicate element concentrations in signal counts per second. Black crosses in the μ-XRF intensity map of S denote μ-XANES measurement points. **Figure S2.** The μ-XRF intensity maps of O, S, Na, Cl, Mg, Al, P, and Si, together with the picture of the measured area in K-3. Color scales indicate element concentrations in signal counts per second. Black crosses in the μ-XRF intensity map of S denote μ-XANES measurement points. **Figure S3.** The XRD spectra of spot 2-1, 2-2, and 2-3, together with the reference spectra of halite, kainite, and leonite. The presence of kainite peaks in spot 2-1 is probably due to contamination of kainite during the sampling by dental drill, because halites only occur as small crystals, making the sampling procedure difficult. **Figure S4.** (a)

Thin section of K-2 under transmitted light. Area filled with resin is indicated as R. (b) Close-up of the red rectangle showing fluid inclusion bands in a halite crystal. (DOCX 4305 kb)

Abbreviations
GC/MS: Gas chromatography/mass spectroscopy; MSC: Messinian Salinity Crisis; XANES: X-ray absorption near edge structure; XRD: X-ray diffraction; XRF: X-ray fluorescence

Authors' contributions
YI, HK, JK, TY, and NO designed the study. YI, HK, JK, TY, FJJE, SL, VM, and MR collected the samples. YI, TY, JK, and YT conducted the experimental work and data analysis. YI wrote the paper with contributions from TY, YT, and NO, and all authors edited and approved the final manuscript.

Availability of data and materials
The datasets supporting the conclusions of this article are included within the article and its additional files.

Competing interests
The authors declare that they have no competing interest.

Author details
[1]Biogeochemistry Program, Japan Agency for Marine-Earth Science and Technology, 2-15 Natsushima, Yokosuka, Kanagawa 237-0061, Japan. [2]Atmosphere and Ocean Research Institute, The University of Tokyo, 5-1-5 Kashiwanoha, Kashiwa, Chiba 277-8564, Japan. [3]Japan Synchrotron Radiation Research Institute/SPring-8, 1-1-1 Kouto, Sayo, Hyogo 679-5198, Japan. [4]The Andalusian Earth Sciences Institute, The Spanish Research Council and the University of Granada, Avda de las Palmeras 4, 18100 Armilla, Spain. [5]Dipartimento di Scienze Chimiche e Geologiche, Università degli Studi di Modena e Reggio Emilia, Via Campi 103, 41125 Modena, Italy. [6]Physics and Earth Science Department, University of Parma, Parco Area delle Scienze 157/A, 43124 Parma, Italy.

References
Bąbel M, Schreiber BC (2014) Geochemistry of evaporites and evolution of seawater. In: Holland H, Turekian K (eds) Treatise on geochemistry, 2nd edn. Elsevier, Oxford, pp 483–560

Bergé JP, Barnathan G (2005) Fatty acids from lipids of marine organisms: molecular biodiversity, roles as biomarkers, biologically active compounds, and economical aspects. In: Ulber R, Le Gal Y (eds) Marine biotechnology I. Advances in Biochemical Engineering/Biotechnology, Springer, Berlin, pp 49–125

Bertini A, Londeix L, Maniscalco R, Di Stefano A, Suc JP, Clauzon G, Gautier F, Grasso M (1998) Paleobiological evidence of depositional conditions in the Salt Member, Gessoso-Solfifera Formation (Messinian, Upper Miocene) of Sicily. Micropaleontology 44:413–433

Birgel D, Guido A, Liu X, Hinrichs KU, Gier S, Peckmann J (2014) Hypersaline conditions during deposition of the Calcare di Base revealed from archaeal di-and tetraether inventories. Org Geochem 77:11–21

Capella W, Flecker R, Hernández-Molina FJ, Simon D, Meijer PT, Rogerson M, Sierro FJ, Krijgsman W (2019) Mediterranean isolation preconditioning the Earth System for late Miocene climate cooling. Sci Rep 9:3795

Decima A, Wezel F (1973) Late Miocene evaporites of the central Sicilian basin, Italy. Initial Reports of the Deep Sea Drilling Project 13:1234–1241

Duggen S, Hoernle K, Van Den Bogaard P, Rüpke L, Morgan JP (2003) Deep roots of the Messinian salinity crisis. Nature 422:602–606

Eglinton G, Hamilton RJ (1967) Leaf epicuticular waxes. Science 156:1322–1335

Francavilla M, Trotta P, Luque R (2010) Phytosterols from *Dunaliella tertiolecta* and *Dunaliella salina*: a potentially novel industrial application. Bioresour Technol 101:4144–4150

Friedman GM, Sanders JE (1978) Principles of sedimentology. Wiley, New York

Garcia-Veigas J, Orti F, Rosell L, Ayora C, Rouchy JM, Lugli S (1995) The Messinian salt of the Mediterranean: geochemical study of the salt from the Central Sicily Basin and comparison with the Lorca Basin (Spain). Bull Soc Géol France 166:699–710

Guido A, Jacob J, Gautret P, Laggoun-Défarge F, Mastandrea A, Russo F (2007) Molecular fossils and other organic markers as palaeoenvironmental indicators of the Messinian Calcare di Base Formation: normal versus stressed marine deposition (Rossano Basin, northern Calabria, Italy). Palaeogeogr Palaeoclim Palaeoecol 255:265–283

Hallsworth JE, Yakimov MM, Golyshin PN, Gillion JL, D'Auria G, de Lima AF, La Cono V, Genovese M, McKew BA, Hayes SL, Harris G, Giuliano L, Timmis KN, McGenity TJ (2007) Limits of life in MgCl$_2$-containing environments: chaotropicity defines the window. Environ Microbiol 9:801–813

Hayes J, Wedeking K, Kaplan I (1983) Precambrian organic geochemistry, Preservation of the record. In: Schopf W (ed) Earth's earliest biosphere. Princeton Univ. Press, Princeton, pp 93–134

Hsü K, Ryan W, Cita M (1973) Late Miocene desiccation of the Mediterranean. Nature 242:240–244

Huang WY, Meinschein W (1979) Sterols as ecological indicators. Geochim Cosmochim Acta 43:739–745

Isaji Y (2018) Revealing the biogeochemical cycles of the hypersaline environments based on the organic geochemical approaches (PhD thesis). The University of Tokyo, Tokyo

Isaji Y, Kawahata H, Kuroda J, Yoshimura T, Ogawa NO, Suzuki A, Shibuya T, Jiménez-Espejo FJ, Lugli S, Santulli A, Manzi V, Roveri M, Ohkouchi N (2017) Biological and physical modification of carbonate system parameters along the salinity gradient in shallow hypersaline solar salterns in Trapani, Italy. Geochim Cosmochim Acta 208:354–367

Isaji Y, Kawahata H, Ogawa NO, Kuroda J, Yoshimura T, Jiménez-Espejo FJ, Makabe A, Shibuya T, Lugli S, Santulli A, Manzi V, Roveri M, Ohkouchi N (2019a) Efficient recycling of nutrients in modern and past hypersaline environments. Sci Rep 9:3718

Isaji Y, Kawahata H, Takano Y, Ogawa NO, Kuroda J, Yoshimura T, Lugli S, Manzi V, Roveri M, Ohkouchi N (2019b) Diazotrophy drives primary production in the organic-rich shales deposited under a stratified environment during the Messinian salinity crisis (Vena del Gesso, Italy). Front Earth Sci 7:85

Ivanovic RF, Valdes PJ, Flecker R, Gutjahr M (2014) Modelling global-scale climate impacts of the late Miocene Messinian Salinity Crisis. Clim Past 10:607–622

Kelly AE (2009) Hydrocarbon biomarkers for biotic and environmental evolution through the Neoproterozoic-Cambrian transition. Dissertation, Massachusetts Institute of Technology, Cambridge

Krijgsman W, Hilgen F, Raffi I, Sierro FJ, Wilson D (1999) Chronology, causes and progression of the Messinian salinity crisis. Nature 400:652–655

Kuroda J, Jiménez-Espejo FJ, Nozaki T, Gennari R, Lugli S, Manzi V, Roveri M, Flecker R, Sierro FJ, Yoshimura T, Suzuki K, Ohkouchi N (2016) Miocene to Pleistocene osmium isotopic records of the Mediterranean sediments. Paleoceanography 31:148–166

Lazar B, Erez J (1992) Carbon geochemistry of marine-derived brines: I. ^{13}C depletions due to intense photosynthesis. Geochim Cosmochim Acta 56:335–345

Lofi J, Sage F, Déverchère J, Loncke L, Maillard A, Gaullier V, Thinon I, Gillet H, Guennoc P, Gorini C (2011) Refining our knowledge of the Messinian salinity crisis records in the offshore domain through multi-site seismic analysis. Bull Soc Geol France 182:163–180

Lowenstein TK, Hardie LA (1985) Criteria for the recognition of salt-pan evaporites. Sedimentology 32:627–644

Lowenstein TK, Schubert BA, Timofeeff MN (2011) Microbial communities in fluid inclusions and long-term survival in halite. GSA Today 21:4–9

Lugli S, Schreiber BC, Triberti B (1999) Giant polygons in the Realmonte mine (Agrigento, Sicily): evidence for the desiccation of a Messinian halite basin. J Sed Res 69:764–771

Manzi V, Gennari R, Lugli S, Roveri M, Scafetta N, Schreiber BC (2012) High-frequency cyclicity in the Mediterranean Messinian evaporites: evidence for solar-lunar climate forcing. J Sed Res 82:991–1005

Manzi V, Lugli S, Roveri M, Schreiber BC (2009) A new facies model for the Upper Gypsum of Sicily (Italy): chronological and palaeoenvironmental constraints for the Messinian salinity crisis in the Mediterranean. Sedimentology 56: 1937–1960

McGenity TJ, Gemmell RT, Grant WD, Stan-Lotter H (2000) Origins of halophilic microorganisms in ancient salt deposits. Environ Microbiol 2:243–250

Naraoka H, Ishiwatari R (2000) Molecular and isotopic abundances of long-chain *n*-fatty acids in open marine sediments of the western North Pacific. Chem Geol 165:23–36

Natalicchio M, Birgel D, Peckmann J, Lozar F, Carnevale G, Liu X, Hinrichs KU, Pierre FD (2017) An archaeal biomarker record of paleoenvironmental change across the onset of the Messinian salinity crisis in the absence of evaporites (Piedmont Basin, Italy). Org Geochem 113:242–253

Oren A (2002) Diversity of halophilic microorganisms: environments, phylogeny, physiology, and applications. J Ind Microbiol Biotechnol 28:56–63

Oren A (2014) The ecology of *Dunaliella* in high-salt environments. J Biol Res Thessalon 21:23

Oro J, Laseter J, Weber D (1966) Alkanes in fungal spores. Science 154:399–400

Ourisson G, Albrecht P (1992) Hopanoids. 1. Geohopanoids: the most abundant natural products on Earth? Acc Chem Res 25:398–402

Rigaudier T, Lécuyer C, Gardien V, Suc JP, Martineau F (2011) The record of temperature, wind velocity and air humidity in the δD and δ^{18}O of water inclusions in synthetic and Messinian halites. Geochim Cosmochim Acta 75: 4637–4652

Rohmer M, Bouvier-Nave P, Ourisson G (1984) Distribution of hopanoid triterpenes in prokaryotes. Microbiology 130:1137–1150

Rouchy JM, Caruso A (2006) The Messinian salinity crisis in the Mediterranean basin: a reassessment of the data and an integrated scenario. Sediment Geol 188–189:35–67

Roveri M, Flecker R, Krijgsman W, Lofi J, Lugli S, Manzi V, Sierro FJ, Bertini A, Camerlenghi A, De Lange G, Govers R, Hilgen FJ, Hübscher C, Meijer PT, Stoica M (2014) The Messinian Salinity Crisis: past and future of a great challenge for marine sciences. Mar Geol 352:25–58

Ryan WB (2009) Decoding the Mediterranean salinity crisis. Sedimentology 56:95–136

Schouten S, Hartgers WA, Lòpez JF, Grimalt JO, Sinninghe Damsté JS (2001) A molecular isotopic study of ^{13}C-enriched organic matter in evaporitic deposits: recognition of CO$_2$-limited ecosystems. Org Geochem 20:277–286

Schouten S, Pavlović D, Sinninghe Damsté JS, de Leeuw JW (1993) Nickel boride: an improved desulphurizing agent for sulphur-rich geomacromolecules in polar and asphaltene fractions. Org Geochem 20:901–909

Shalev N, Lazar B, Köbberich M, Halicz L, Gavrieli I (2018) The chemical evolution of brine and Mg-K-salts along the course of extreme evaporation of seawater–an experimental study. Geochim Cosmochim Acta 241:164–179

Shen J, Yuan L, Zhang J, Li H, Bai Z, Chen X, Zhang W, Zhang F (2011) Phosphorus dynamics: from soil to plant. Plant Physiol 156:997–1005

Simon D, Meijer PT (2017) Salinity stratification of the Mediterranean Sea during the Messinian crisis: A first model analysis. Earth Planet Sci Lett 479:366–376

Sinninghe Damsté JS, Frewin NL, Kenig F, De Leeuw JW (1995b) Molecular indicators for palaeoenvironmental change in a Messinian evaporitic sequence (Vena del Gesso, Italy). I: Variations in extractable organic matter of ten cyclically deposited marl beds. Org Geochem 23:471–483

Sinninghe Damsté JS, Kenig F, Koopmans MP, Köster J, Schouten S, Hayes J, de Leeuw JW (1995a) Evidence for gammacerane as an indicator of water column stratification. Geochim Cosmochim Acta 59:1895–1900

Spiro C, Wong J, Lytle F, Greegor R, Maylotte D, Lamson S (1984) X-ray absorption spectroscopic investigation of sulfur sites in coal: Organic sulfur identification. Science 226:48–50

Stewart FH (1963) Marine evaporites. Data of Geochemistry, sixth ed. USGS professional paper 440-Y

Summons RE, Bradley AS, Jahnke LL, Waldbauer JR (2006) Steroids, triterpenoids and molecular oxygen. Philos Trans R Soc Lond B Biol Sci. 361:951–968

Sutton SR, Bertsch PM, Newville M, Rivers M, Lanzirotti A, Eng P (2002) Microfluorescence and microtomography analyses of heterogeneous earth and environmental materials. Rev Mineral Geochem 49:429–483

Takishita K, Chikaraishi Y, Leger MM, Kim E, Yabuki A, Ohkouchi N, Roger AJ (2012) Lateral transfer of tetrahymanol-synthesizing genes has allowed

multiple diverse eukaryote lineages to independently adapt to environments without oxygen. Biol Direct 7:5

Tamenori Y, Morita M, Nakamura T (2011) Two-dimensional approach to fluorescence yield XANES measurement using a silicon drift detector. J Synchrotron Rad 18:747–752

Tamenori Y, Yoshimura T, Luan NT, Hasegawa H, Suzuki A, Kawahata H, Iwasaki N (2014) Identification of the chemical form of sulfur compounds in the Japanese pink coral (*Corallium elatius*) skeleton using μ-XRF/XAS speciation mapping. J Struct Biol 186:214–223

Ten Haven HL, De Leeuw JW, Schenck PA (1985) Organic geochemical studies of a Messinian evaporitic basin, northern Apennines (Italy) I: Hydrocarbon biological markers for a hypersaline environment. Geochim Cosmochim Acta 49:2181–2191

Volkman JK (2005) Sterols and other triterpenoids: source specificity and evolution of biosynthetic pathways. Org Geochem 36:139–159

Warren JK (2016) Evaporites: A geological compendium. Springer, New York

Werne JP, Hollander DJ, Lyons TW, Sinninghe Damsté JS (2004) Organic sulfur biogeochemistry: recent advances and future research directions. Geol Soc Spec Pap 379:135–150

Yoshimura T, Kuroda J, Lugli S, Tamenori Y, Ogawa NO, Jiménez-Espejo FJ, Isaji Y, Roveri M, Manzi V, Kawahata H, Ohkouchi N (2016) An X-ray spectroscopic perspective on Messinian evaporite from Sicily: sedimentary fabrics, element distributions, and chemical environments of S and Mg. Geochem Geophys Geosyst 17:1383–1400

Yoshimura T, Tamenori Y, Iwasaki N, Hasegawa H, Suzuki A, Kawahata H (2013) Magnesium K-edge XANES spectroscopy of geological standards. J Synchrotron Rad 20:734–740

Yoshimura T, Tamenori Y, Takahashi O, Nguyen LT, Hasegawa H, Iwasaki N, Kuroyanagi A, Suzuki A, Kawahata H (2015) Mg coordination in biogenic carbonates constrained by theoretical and experimental XANES. Earth Planet Sci Lett 421:68–74

Publisher's Note

Springer Nature remains neutral with regard to jurisdictional claims in published maps and institutional affiliations.